

Wave propagation simulation and its wavelet package analysis for debonding detection of circular CFST members

Bin Xu^{*1,2}, Hongbing Chen^{3a} and Song Xia^{4b}

¹College of Civil Engineering, Huaqiao University, Xiamen, Fujian 361021, China

²Key Laboratory for Structural Engineering and Disaster Prevention of Fujian Province (Huaqiao University), Xiamen, Fujian 361021, China

³College of Civil Engineering, Hunan University, Changsha, Hunan 410082, China

⁴School of Electric and Information Engineering, Xi'an Jiaotong University, 28 Xianning West Road, Xi'an, Shaanxi, 710049, P.R. China

(Received June 24, 2016, Revised October 20, 2016, Accepted October 27, 2016)

Abstract. In order to investigate the interface debonding defects detection mechanism between steel tube and concrete core of concrete-filled steel tubes (CFSTs), multi-physical fields coupling finite element models constituted of a surface mounted Piezoceramic Lead Zirconate Titanate (PZT) actuator, an embedded PZT sensor and a circular cross section of CFST column are established. The stress wave initiation and propagation induced by the PZT actuator under sinusoidal and sweep frequency excitations are simulated with a two dimensional (2D) plain strain analysis and the difference of stress wave fields close to the interface debonding defect and within the cross section of the CFST members without and with debonding defects are compared in time domain. The linearity and stability of the embedded PZT response under sinusoidal signals with different frequencies and amplitudes are validated. The relationship between the amplitudes of stress wave and the measurement distances in a healthy CFST cross section is also studied. Meanwhile, the responses of PZT sensor under both sinusoidal and sweep frequency excitations are compared and the influence of debonding defect depth and length on the output voltage is also illustrated. The results show the output voltage signal amplitude and head wave arriving time are affected significantly by debonding defects. Moreover, the measurement of PZT sensor is sensitive to the initiation of interface debonding defects. Furthermore, wavelet packet analysis on the voltage signal under sweep frequency excitations is carried out and a normalized wavelet packet energy index (NWPEI) is defined to identify the interfacial debonding. The value of NWPEI attenuates with the increase in the dimension of debonding defects. The results help understand the debonding defects detection mechanism for circular CFST members with PZT technique.

Keywords: piezoceramics; concrete-filled steel tube; debonding defect; identification; wave propagation method; numerical simulation; wavelet packet analysis

1. Introduction

Due to advanced mechanical behaviors, including excellent energy dissipation capacity under strong dynamic excitations such as earthquakes, high load-carrying capability, economic benefits and convenience in construction process, concrete-filled steel tube (CFST) structures have been extensively adopted as major load-carrying components in large-scale structures, such as super high-rise buildings, long span bridges, large-scale hydraulic projects, harbor engineering and subway stations (Han, Li *et al.* 2014, Xue, Li *et al.* 2012). Because of the increasing needs in load carrying capacity, the cross-section dimension of CFST members grows dramatically and the CFSTs with

irregular cross-section shape have been employed in practice (Liu, Ho *et al.* 2012). The effective bonding condition between the steel tube and concrete core plays key role in ensuring the load-carrying capacity and the ductility of CFST members (Xue, Li *et al.* 2012). However, the interface debonding between steel tube and concrete core easily occurs due to the obvious non-uniform distribution of temperature during hydration and hardening process, shrinkage and creep of concrete core together with influence of horizontal diaphragm if no reliable anchorage is available. Unfortunately, the interface debonding detection is still a challenging task because most of the existing conventional non-destructive testing (NDT) technologies cannot be employed.

The conventional NDT technologies, including ultrasound method, ray method and ground penetrating radar technology, electromagnetic method (EM) etc., have their own drawbacks and are not applicable for the interface debonding detection of CFST members (China Engineering Construction standardization association, 2000). For example, even though the EM method can be employed to detect the interface debonding for fiber reinforced polymer (FRP)-jacketed concrete structures (Feng, De Flaviis *et al.*

*Corresponding author, Professor

E-mail: binxu@hqu.edu.cn

^a Ph.D. Candidate

E-mail: chb@hnu.edu.cn

^b Ph.D.

E-mail: xia.emrl@qq.com

2002), it is not suitable for the debonding detection of CFST structures since the shielding effect of steel tube which makes the penetration of electromagnetic wave through the metallic media impossible. However, recently, the structural damage detection technologies based on smart materials such as piezoelectric material have gradually become the most attractive approaches for civil engineering structures. Piezoceramic Lead Zirconate Titanate (PZT) material with low cost, fast response, wide response frequency range and good linearity properties has been recognized as one of the most promising materials in structural health monitoring (SHM) or damage detection for civil engineering structures. Recently, a series of experimental studies on the stress monitoring and damage identification for reinforced concrete (RC) beams, columns and shear walls under pseudo-static loads, cyclic loads and earthquake excitations using PZT patches have been carried out (Bhalla and Soh 2004, Zhao and Li 2006, 2009, Song, Gu *et al.* 2007, Laskar, Gu *et al.* 2009, Gu, Moslehly *et al.* 2010, Moslehly, Nestorovic *et al.* 2010). Song, Gu *et al.* (2008) presented a tutorial and a state-of-the-art review on the PZT-based smart aggregates (SAs) as multifunctional sensors in RC structures. Yan, Sun *et al.* (2009) applied SAs in the SHM for RC structures and provided a damage evaluation method based on signal energy attenuation. Jung, Kundu *et al.* (2002) employed lamb wave to detect the internal defects, cracks and bonding properties between concrete and steel rebars. By utilizing embedded PZT based functional elements (EPFEs), Meng, Yan *et al.* (2010) proposed a crack damage detection for concrete beam based on PZT wave method. Meanwhile, for the overweight vehicle-bridge collision monitoring, a system using piezoelectric transducers was proposed by Olmi, Gu *et al.* (2007). Michaels and Michaels (2007) adopted the spatial distribution array of single PZT transducer to achieve the integrity detection of the plate-type structures over large areas.

In addition to experimental studies, numerical analysis on the investigation on the mechanism of PZT based wave propagation measurement and the electro-mechanical impedance (EMI) measurement NDT methods using finite element method (FEM) have been carried out. Markovic, Nestorovic *et al.* (2015) simulated the stress wave propagation in a RC beam with ABAQUS and the wave propagation properties in components with and without damage were compared. However, the piezoelectric effect of PZT materials and the coupling effect between the PZT patches and the structure were not considered directly. Wu and Chang (2006a, b) performed numerical simulation with Flex software to evaluate the response of PZT sensors embedded in concrete and proposed a debonding detection algorithm for RC structures. Aiming at quantitative assessment of crack size in aluminium plates, numerical simulation was employed to analyze the interaction of Lamb wave modes with different excitation frequencies. The wave transmission, reflection and diffraction due to cracks were significant and the crack size was quantitatively evaluated through the relationship between crack length and the predefined reflection/transmission coefficient (Lu, Ye *et al.* 2008). In addition, the finite element analysis with

ABAQUS was also carried out to simulate the propagation simulation for Lamb wave in composite laminates (Yang, Ye *et al.* 2006). In the field of numerical simulation study on the EMI for SHM, combined with the experimental research and numerical simulations, Morikawa, Gama *et al.* (2005) carried out a numerical study with finite element method to determine a correlation between the PZT sensor response and defect depth in beams using PZT impedance method. Park, Ahmad *et al.* (2006) constructed electro-mechanical coupling finite element models with ANSYS to detect multiple cracks for concrete structures successfully with an evaluation index called as root mean square deviation (RMSD). Wang *et al.* employed EMI to monitor the strength of concrete and carried out numerical and experimental studies on damage detection for a concrete beam based on PZT admittances and correlation coefficient (Wang, Song *et al.* 2013, 2014).

In recent years, a large number of super high-rise buildings and long span bridges employ CFST members with different regular or irregular cross section shapes as vertical load-carrying components (Liu, Ho *et al.* 2012). It is critical to develop an effective interface debonding detection approach for CFST structure members to meet the engineering needs. Recently, an active NDT system based on PZT transducers has been developed to effectively detect the debonding defects of CFST members, validated experimentally and applied in practice for the SHM of super high-rise buildings successfully in China (Xu, Li *et al.* 2012, 2013, Xu, Li *et al.* 2013).

Fig. 1 shows the set up of the proposed active interface debonding defect detection system based on the wave propagation measurement with PZT technology for a circular CFST member. A PZT patch is surface-mounted on the circular steel tube as an actuator and a PZT patch is embedded in concrete core as a sensor to measure the stress wave propagating from the PZT actuator. PZT actuator is excited with an arbitrary function generator and the response of PZT sensor is recorded with a high speed data acquisition system. By analyzing the PZT sensor measurement, the interface debonding is detected. The debonding length means the length of the interface debonding between the circular steel tube and concrete core in the circumferential direction of the steel tube and the depth of the interface debonding defect is the dimension of the debonding defect in the radius direction.

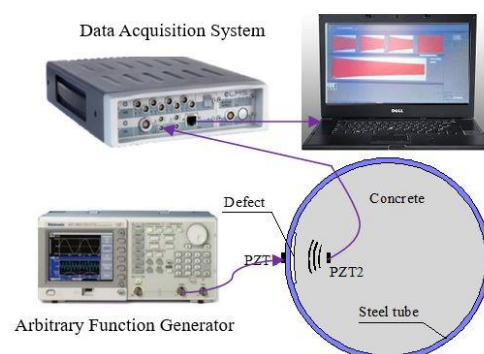


Fig. 1 Interface defect detection system based on wave propagation measurement using PZT technology

In order to validate the findings from experimental studies by the authors on the interfacial debonding detection with PZT patches and to illustrate the effect of the interface debonding on the stress wave propagation characteristics in the cross section of CFST structure members without and with debonding defects, in this study, multi-physical coupling models composed of a surface mounted PZT actuator, an embedded PZT sensor and a circular CFST column with and without interface debonding defects are established with COMSOL software using two-dimensional (2D) plain strain elements considering the coupling effects between the piezoceramics material and the circular CFST member and the piezoelectric behavior of PZT materials. After verifying the linearity and stability of the proposed multi-physical coupling model, numerical simulation on the stress wave propagation at the interface and within the cross section of the circular CFST member without and with interface debonding defects is carried out. The effects of interface debonding on the properties of stress wave propagation, including propagation path, arriving time of head wave and attenuation trend are discussed in detail. The sensitivity of the stress wave measurement on the interface debonding length and depth is discussed. The energy loss of output voltage signals caused by interface debonding defects is discussed based on wavelet packet analysis. An energy index (EI) based on the wavelet packet analyses is defined and employed to detect the interface defects. The results are helpful to understand the debonding defects detection mechanism based on wave propagation measurement using PZT technology for CFST structural members.

2. Multi-physical PZT-CFST coupling finite element model

2.1 Control equations of stress wave propagation in solid

The elastic wave propagation in solid is mainly guided by the conservation law of force, satisfying constitutive law of elastic materials and the basic assumptions of elastic mechanics as shown in the following equations (Mo 2007, Wang 2013).

$$\rho \frac{\partial^2 \mathbf{u}}{\partial t^2} = \nabla \cdot \mathbf{s} + \mathbf{F}_v \quad (1)$$

$$\nabla = \left(\frac{\partial}{\partial x} + \frac{\partial}{\partial y} + \frac{\partial}{\partial z} \right)^T \quad (2)$$

$$\mathbf{s} = \mathbf{S}_0 + \mathbf{C} : (\boldsymbol{\varepsilon} - \boldsymbol{\varepsilon}_0) \quad (3)$$

$$\boldsymbol{\varepsilon} = \frac{1}{2} [(\nabla \mathbf{u})^T + (\nabla \mathbf{u})] \quad (4)$$

where ρ stands for the density of elastic materials, \mathbf{u} denotes the displacement vector, t is the time variable, \mathbf{S} and \mathbf{S}_0 are the stress tensor and initial stress, ∇ is the gradient

operator, $\boldsymbol{\varepsilon}$ and $\boldsymbol{\varepsilon}_0$ represent strain and the initial strain, \mathbf{F}_v is the external load vector, and \mathbf{C} refers to elastic matrix.

2.2 Control equations of PZT materials

The PZT materials contain two kinds of physical characteristics, including piezoelectric effect and solid mechanics. So, the mechanical equilibrium condition and the charge conservation equation should be satisfied simultaneously in transient dynamic analysis. The mechanical equilibrium equations of PZT are similar to that of general solid materials such as CFST members as discussed above and the charge conservation equations can be described as follows (COMSOL Inc. 2015, Mo 2007, Wang 2013)

$$\mathbf{s} = \mathbf{S}_0 + c_E : (\boldsymbol{\varepsilon} - \boldsymbol{\varepsilon}_0) - e^T \mathbf{E} \quad (5)$$

$$\mathbf{D} = \mathbf{D}_r + e(\boldsymbol{\varepsilon} - \boldsymbol{\varepsilon}_0) + \boldsymbol{\varepsilon}_{0,vac} \boldsymbol{\varepsilon}_{rS} \mathbf{E} \quad (6)$$

$$\nabla \cdot \mathbf{D} = \rho_V \quad (7)$$

$$\mathbf{E} = -\nabla V \quad (8)$$

where c_E is elastic matrix, e is the piezoelectric stress constant matrix, \mathbf{D} and \mathbf{D}_r stand for the electric displacement and the residual electric displacement, ρ_V is charge density, \mathbf{E} is the electric field strength and V refers to voltage. $\boldsymbol{\varepsilon}_{0,vac}$ and $\boldsymbol{\varepsilon}_{rS}$ are dielectric constant in vacuum and relative dielectric constant.

The transformation relationship of control equations of PZT materials between the stress-charge type and the strain-charge type can be presented as follows

$$c_E = s_E^{-1} \quad (9)$$

$$e = d s_E^{-1} \quad (10)$$

$$\boldsymbol{\varepsilon}_{rS} = \boldsymbol{\varepsilon}_{rT} - d s_E^{-1} d^T / \boldsymbol{\varepsilon}_{0,vac} \quad (11)$$

Where S_E refers to flexible matrix, d denotes the coupling matrix matrix, and $\boldsymbol{\varepsilon}_{rT}$ is relative dielectric constant.

2.3 Boundary conditions

For the plane analysis in semi-infinite space, low reflective boundary is employed to simulate the infinite boundary conditions

$$\boldsymbol{\sigma} \cdot \mathbf{n} = -\mathbf{d}_i \frac{\partial \mathbf{u}}{\partial t} \quad (12a)$$

$$\mathbf{d}_i = \mathbf{d}_i(\rho, c_s, c_p) \quad (12b)$$

where $\boldsymbol{\sigma}$ is the stress matrix and \mathbf{n} is the normal vectors of boundary, \mathbf{d}_i is a function of density ρ , c_s and c_p . c_s is the shear wave velocity and c_p represents longitudinal wave

velocity.

The continuity conditions of the stress and displacement components should be satisfied at the interface between the piezoelectric material and CFST member. Furthermore the continuity conditions can be expressed as follows

$$\mathbf{n}_i^I \boldsymbol{\sigma}_{ij}^I = \mathbf{n}_i^{II} \boldsymbol{\sigma}_{ij}^{II} \quad (13)$$

$$\mathbf{u}_j^I = \mathbf{u}_j^{II} \quad (14)$$

$$\mathbf{n}_i^I D_i^I = \mathbf{n}_i^{II} D_i^{II} \quad (15)$$

where superscript ‘‘I’’ and ‘‘II’’ indicate the variables for PZT patches and CFST components respectively. σ_{ij} is stress of the nodes at the interface and \mathbf{n}_i means the component of unit normal vector. D_i is the electric displacement intensity.

Considering the piezoelectric effect of PZT and the coupling effect between the PZT material and CFST member, transient dynamic analysis and harmonic response analysis under sweep frequency signals and sinusoidal signals are carried out respectively to simulate the stress wave propagation in the CFST cross section without and with interface debonding defects.

2.5 The establishment of the multi-physical PZT-CFST coupling FEM model

2.5.1 Cross section of circular CFST member with PZT actuator and sensor

In this paper, the stress wave propagation at the interface and within the cross section of a circular CFST member is simulated. The multi-physical PZT-CFST coupling FEM model is discretized with 2D plane strain elements and the propagation of stress wave along the thickness direction of the CFST member is not considered.

Fig. 2 shows the cross section of the circular CFST member and the installation of PZT actuator and sensor. As shown in Fig. 2, the outer diameter of the circular steel tube is 400 mm and the thickness of the steel tube is 5 mm. PZT1 mounted on the outer surface of the circular steel tube works as an actuator and PZT2 embedded in concrete core serves as a sensor. The dimension of both PZT ceramics as actuator and sensor is 10mm by 10mm with a thickness of 0.3 mm. The distance between PZT2 and PZT1 is 80 mm.

In order to investigate the influence of interface debonding defect dimension on the propagation properties of stress wave within the cross section of CFST members, a total of six interface debonding scenarios with different length and depth are considered as shown in Table 1.

Table 1 Setting for interface debonding defects

No.	Defect length × depth (mm×mm)	No.	Defect length × depth (mm×mm)
1	50×3	4	50×1
2	100×3	5	50×3
3	150×3	6	50×5

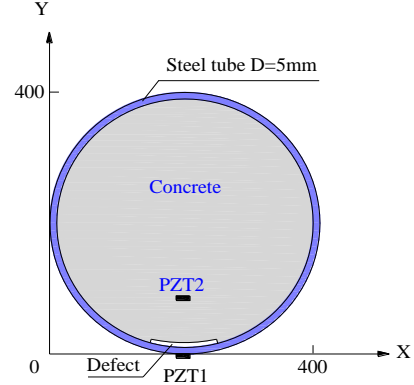


Fig. 2 Cross section of a CFST member with PZT patches as actuator and sensor (unit: mm)

2.5.2 Material parameters definition

For simplicity and without loss of generality, steel and concrete materials are treated as elastic homogeneous medium in the stress wave propagation analysis. The material parameters of the steel and concrete are shown in Table 2. The thickness direction of piezoelectric ceramics is specified as the polarization direction. The flexibility matrix, coupling matrix and relative dielectric constant matrix of the PZT material employed in this study as actuator and sensor are shown in Eqs. (16)-(18) respectively.

Flexibility matrix

$$s_E = \begin{bmatrix} 16.4 & -5.7 & -7.2 & 0 & 0 & 0 \\ -5.7 & 16.4 & -7.2 & 0 & 0 & 0 \\ -7.2 & -7.2 & 18.8 & 0 & 0 & 0 \\ 0 & 0 & 0 & 47.5 & 0 & 0 \\ 0 & 0 & 0 & 0 & 47.5 & 0 \\ 0 & 0 & 0 & 0 & 0 & 44.3 \end{bmatrix} \times 10^{-12} / Pa \quad (16)$$

Coupling matrix

$$d = \begin{bmatrix} 0 & 0 & 0 & 0 & 0 & 5.84 \\ 0 & 0 & 0 & 5.84 & 0 & 0 \\ -1.71 & -1.71 & 3.74 & 0 & 0 & 0 \end{bmatrix} \times 10^{-10} C / N \quad (17)$$

Relative dielectric constant matrix

$$\varepsilon_{r,s} = \begin{bmatrix} 1730 & 0 & 0 \\ 0 & 1730 & 0 \\ 0 & 0 & 1700 \end{bmatrix} \quad (18)$$

The dielectric constant in vacuum is $\varepsilon_{0,voc} = 8.84 \times 10^{-12} C / m$ and the density of the PZT material is $7,500 \text{ kg/m}^3$.

2.5.3 Meshing of the coupling system and time step setting

For PZT based interface debonding detection with wave propagation method, in order to detect small dimension interface debonding, excitation signals with high frequency are preferred.

Table 2 Material properties

Material	Elastic Modulus (Pa)	Density (kg/m ³)	Poisson's ratio	Shear modulus (Pa)	Longitudinal wave velocity (m/s)	Shear wave velocity (m/s)
Steel	2.1E+11	7800	0.3	8.0E+10	5151.5	3194.9
Concrete	3.5E+10	2400	0.2	1.4E+10	3791.4	2447.4

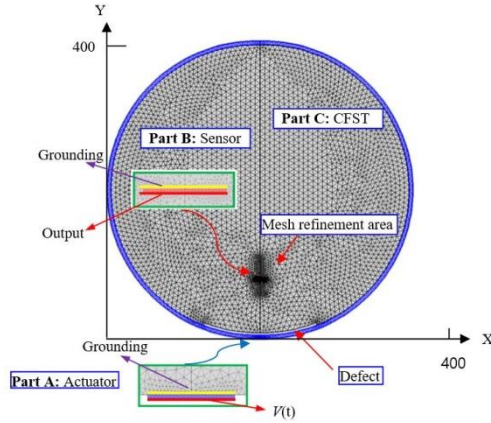


Fig. 3 Meshing of the PZT-CFST coupling system (20 kHz)

High frequency wave has short wave length. Thus, a fine meshing is required in order to illustrate the wave propagation with high-precision. Generally speaking, it is better to represent each wavelength with 10-12 element nodes. Second-order element and higher order element are usually adopted for piezo-mechanical coupling analysis in COMSOL software (COMSOL Inc. 2015). For second-order element, the following formulas should be satisfied.

$$h \leq \lambda / 5 \quad (19)$$

where h is the maximum element size and λ is the maximum wavelength.

Usually, the magnitude of Courant-Friedrichs-Lewy (CFL) could take the value of 0.2, and the integral time step dt can be determined according to the following Eqs. (20) and (21)

$$CFL = c_{\min} \times \frac{dt}{h} = \min(c_s, c_p) \times \frac{dt}{h} = 0.2 \quad (20)$$

$$dt = CFL \times h / \min(c_s, c_p) \quad (21)$$

In this study, an adaptive triangular plane strain element is employed in meshing the multi-physical PZT-CFST coupling model. The element size and integral time step are adjusted automatically corresponding to the excitation frequency. Here, the frequency of 20 kHz is taken as an example and the corresponding meshing for the CFST member and PZT ceramics is presented in Fig. 3. Refined mesh for both PZT patches and steel tubes is used to acquire higher computational accuracy in the transient

dynamic analysis.

As shown in Fig. 3, the PZT actuator is mounted to the exterior surface of the circular steel tube and the PZT sensor is embedded in concrete core. The fine meshing around the PZT actuator and sensor is described in detail in Part A and Part B, respectively. At the bonding interfaces, in order to ensure the deformation continuity between the PZT patches and CFST member, the "sharing nodes" method is adopted and the same method is also employed at the interfaces between steel tube and concrete core. The stress wave induced by the PZT actuator penetrates through the steel tube into the concrete core, and voltage signals generate at the terminal of embedded PZT sensor due to the stress wave excitation along its polarization direction. The interface debonding is mimicked by removing some concrete elements from the concrete core.

As shown in Fig. 3, the surface voltages of the PZT actuator are set to $V(t)$ and 0V respectively to simulate input voltage signal and grounding. The charge of output terminal and the initial voltage of PZT sensor are specified to zero to keep the sensor in the state of electrical open circuit.

In order to simulate the attenuation of the stress wave in practical structures, Rayleigh damping is employed in analysis and the parameters can be obtained according to Eqs. (22) and (23).

$$\alpha_{dM} = 4\pi\xi \frac{f_1 f_2}{f_1 + f_2} \quad (22)$$

$$\beta_{dK} = \frac{\xi}{\pi(f_1 + f_2)} \quad (23)$$

where α_{dM} and β_{dK} are the damping coefficients. ξ is the damping ratio and takes the value of 0.025 in this study, f_1 and f_2 are the first and the second natural frequency of the CFST structure member.

3. Overall stress wave propagation pattern in the cross section of circular CFST under impulse excitation

At first, in order to understand the overall stress wave propagation pattern in the cross section of the circular CFST member, numerical simulation on the initiation and propagation of stress wave in the cross section of the circular CFST members without and with debonding defects is carried out and compared at different time instants in this section.

Considering the geometrical dimensions including the thickness and the width and length of the surface mounted PZT actuator which are much smaller than that of the circular CFST member, in the numerical analysis on the overall stress wave propagation in the cross section of CFST structure members, the excitation induced by the PZT actuator is simplified as a concentrated force acting on the outer surface of the circular steel tube along the polarization direction.

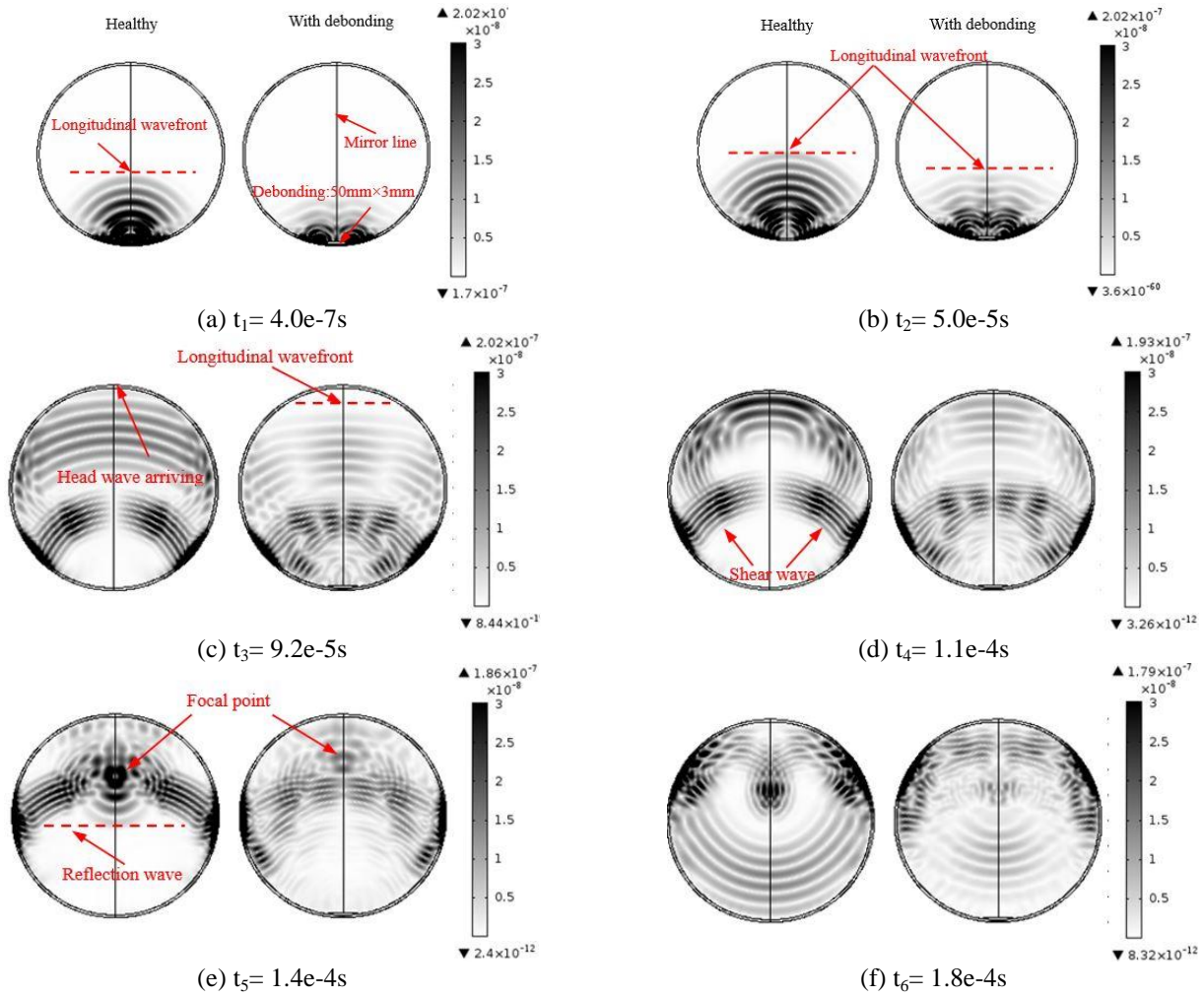


Fig. 4 Wave field snapshots at different time instants (m)

In this study, the impulse voltage shown in Eq. (24) is adopted to discuss the stress wave propagation in the cross section of the CFST members without and with interfacial debonding defects induced by the PZT actuator. The frequency is set to 5 MHz.

$$F(t) = \begin{cases} F_0 \sin(2\pi ft) \left(\sin\left(\frac{2\pi ft}{5}\right) \right)^2, & t < \frac{5}{2f} \\ 0, & t \geq \frac{5}{2f} \end{cases} \quad (24)$$

where $F(t)$ and F_0 are excitation force and its amplitude, f stands for the frequency of signal.

A circular CFST specimen with a debonding defect of 50 mm in length and 3mm in thickness is considered as an example. The amplitude of impulse force excitation is set to 1e-6N and the frequency takes the value of 200 kHz. Fig. 4 shows the comparison of the stress wave propagation pattern in the cross section of the circular CFST members without and with interface debonding defects at different time instants. The difference in the stress wave propagation patterns, the wave propagation delay and the interaction of the reflection of longitudinal wave, boundary reflections and shear waves is clear. The corresponding description in

detail on the wave propagation characteristics are shown in Table 3.

4. Local effect of interface debonding on stress wave initiation and propagation considering the coupling and piezoelectric effects

In order to present a local description on the stress wave initiation and propagation at the interface of the circular CFST member without and with interface debonding in detail, numerical simulation on the stress wave initiation and propagation in a local region, the Part A, as shown in Fig. 3, excited by the surface mounted PZT actuator, is carried out. Sinusoidal signal shown in Eq. (25) is employed as the input signal applied to the PZT actuator in the multi-physical coupling model.

$$V(t) = V_0 \sin(2\pi ft) \quad (25)$$

where $V(t)$ and V_0 refer to excitation voltage signal and its amplitude.

Table 3 Wave field descriptions at different time instants

No.	Time instant	Wave field descriptions	
		Healthy specimen	Specimen with debonding defect
1	$t_1=4.0e-5s$	After passing through the interface between steel tube and concrete core, the transmission wave continues to spread forward in concrete core with a clear waveform.	Caused by the existence of debonding defect, the wave diffraction occurs during the propagation with an ambiguous waveform and delayed wave front
2	$t_2=5.0e-5s$	The stress wave continues spreading forward and the wave front becomes apparent.	After diffraction, the stress wave re-converges together and an inapparent wave front appears.
3	$t_3=9.2e-5s$	The longitudinal wave arrives at the boundary of opposite side and the shear wave shows up clearly. Besides, the propagation velocity of shear wave in steel tube is slightly higher than that in concrete.	The longitudinal wave continues to move forward, and the waveform of shear wave is clearly visible.
4	$t_4=1.1e-4s$	After arriving at the boundary, the longitudinal wave starts to reflect and then focus on one point together with boundary reflections and shear waves. Moreover, the re-converging process is clearly visible.	The focusing of the reflection of longitudinal wave, boundary reflections and shear waves is unclear and the waveform turns to be obscure.
5	$t_5=1.4e-4s$	The reflected stress wave continues to propagate forward after superimposition at the focal point. Wave front line and wave shape are clearly visible.	A relatively clear wave front appears after superposition and the amplitude is reduced obviously.

The sinusoidal excitation signal has an amplitude of 8 V and a frequency of 5 MHz. Because the wave propagates across the upper and the two side boundaries directly in the whole model, the three boundaries of the Part A are defined as low-reflection boundaries in order to reduce the influence of reflection wave.

The comparison of the initiation and propagation of stress wave at the interface of CFST members without and with interface debonding defect is illustrated in Fig. 5. The transmission and reflection waves are clearly visible at the interface between steel tube and concrete core. The waveforms of longitudinal and shear waves are clear in healthy specimen and the propagation of the longitudinal wave is faster than that of the shear wave. For the CFST member with interface debonding, due to the existence of the interface debonding defect, the stress wave has to propagate along the steel tube at first and bypass the interface debonding defect, which induces significant wave diffraction phenomena. Thus, owing to the diffraction phenomena caused by interface debonding defect, the stress

wave propagation path is prolonged as a result. At the same time, the wave amplitude attenuates obviously accompanied with a delayed wave front. As shown in Figs. 5(c)-5(f), for the circular CFST member with interface debonding defect, the wave propagates from two ends of the interface debonding defect and enters the concrete core due to the existence of the interface debonding defect.

Results indicate that the stress wave penetrates through the steel tube and propagates into the concrete core, which means that the stress wave induced by PZT actuator can be employed to “see through” the cross section of CFST structure members to achieve interface debonding defect detection. The stress wave based interface debonding detection approach overcomes the shortages of the EM method, which is employed in the interface debonding detection for fiber reinforced polymer (FRP)-jacketed concrete structures but has difficulties in debonding detection for CFST structures due to the shielding effect of steel plate (Feng, De Flaviis *et al.* 2002).

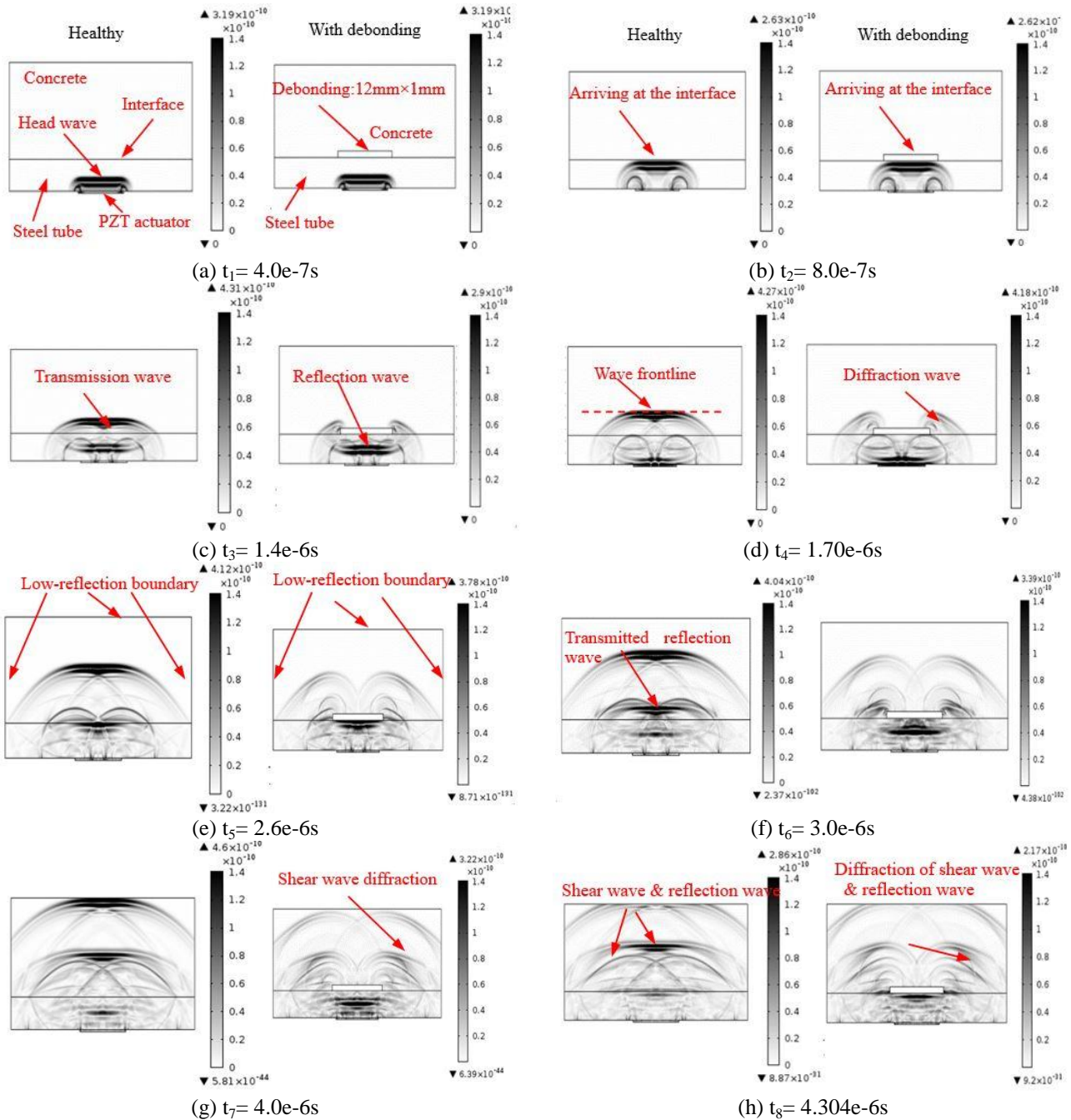


Fig. 5 Comparison of the stress wave fields at the interface of CFST without and with interface debonding defects

5. Linearity and stability of PZT measurements and sensitivity analysis

5.1 Linearity of the embedded PZT sensor response

The linearity and the stability of the multi-physical coupling model considering the piezoelectric effect and the coupling effect between the PZT and the circular steel tube and the concrete core are studied.

In this section, the voltage responses of the PZT sensor embedded in a healthy circular CFST specimen under sinusoidal voltage excitation with different amplitudes are

investigated to illustrate the relationship between the input amplitudes and output voltage signals. Here, the frequency is set to 20 kHz and the voltage amplitudes, including 10 V, 20 V, 30 V and 40 V, are taken into consideration respectively.

Fig. 6 shows the output voltage of the embedded PZT sensor when input voltage amplitude changes. Fig. 7 shows the relationship between the input amplitude and that of the output signals. As shown in Figs. 6 and 7, the amplitude of the output voltages increases linearly with that of the input voltages, while the waveforms keep consistent with each other.

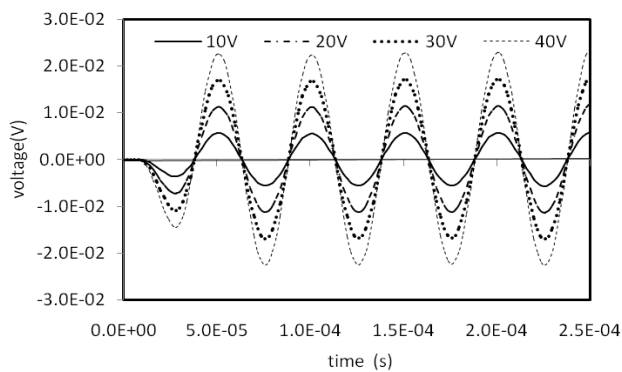


Fig. 6 Output voltage when input voltage amplitude changes

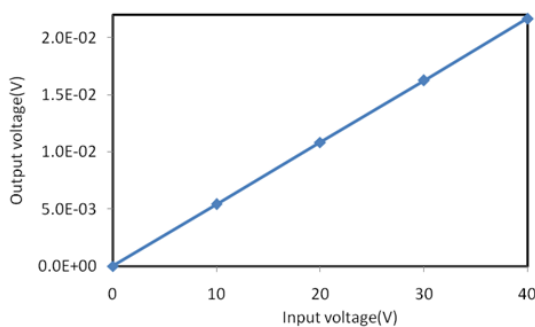


Fig. 7 The relationship between the amplitudes of input and output signals

5.2 Effect of excitation frequency

Because the sensitivity of different wavelength to the dimensions of debonding defect is different, it is important to investigate the effect of different excitation signals on the response of embedded PZT sensor. The response of the embedded PZT sensor is simulated under sinusoidal excitations with different frequencies in this section. In the simulation, the amplitude of sinusoidal voltage is set to 8V and the frequencies are specified as 20 kHz, 30 kHz, 40 kHz, respectively. Fig. 8 shows the output voltage time series corresponding to different excitation frequencies. As shown in Fig. 8, the higher the excitation frequency is, the more remarkable the signal attenuation is.

5.3 Embedded PZT sensor response attenuation with measurement distance

In practice, it is important to install PZT sensors at suitable locations within CFST members by considering the attenuation of stress wave during the propagation in concrete. Therefore, attenuation of embedded PZT sensor response with measurement distance is studied here numerically.

For the attenuation of stress wave in concrete, classical exponential attenuation law has been proposed. However, for CFST structures, there are two kinds of materials with

different properties are employed. Unlike the wave propagation in concrete structures, reflection wave occurs at the interface since the acoustical impedance and wave velocity in steel tube and concrete are different. By the multi-physical fields coupling model, the attenuation trend of stress wave in CFST is investigated by analyzing the voltage signals obtained from the embedded PZT sensor at different distances from the PZT actuator. Here, the amplitude of the sinusoidal excitation voltage is set to 10V and the frequency takes the value of 20 kHz. Generally, for the circular CFST member studied in this paper, the distance from the PZT actuator to the PZT sensor usually does not exceed the radius of the specimen in practice. So, in this simulation the distances take the values of 8 cm, 12 cm, 16 cm and 24 cm, which is a little bit larger than the radius of the CFST specimen.

Fig. 9 shows the time domain response of the embedded PZT sensors with different distances from the PZT actuator and Fig. 10 shows the relationship between the amplitude of the PZT sensor measurement with the distance from the surface mounted PZT actuator. It is clear that the PZT sensor response amplitude attenuates significantly with the increase in the distance between the PZT actuator and sensor.

As shown in Fig. 10, the attenuation of the PZT sensor voltage amplitudes can be fitted as an exponential equation when the distance is no more than 24 cm. While ignoring the influence of the thin steel plate, the attenuation law of PZT sensor response voltage amplitudes can be described by the following equation (Wang 2013)

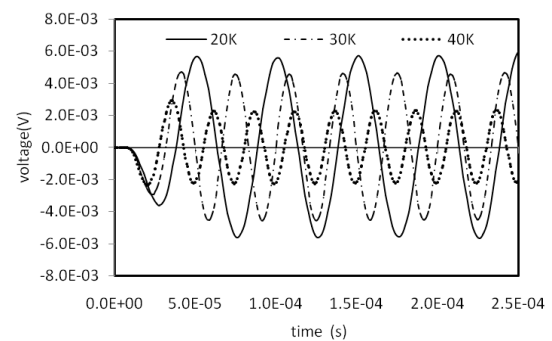


Fig. 8 Output voltages corresponding to different excitation frequencies

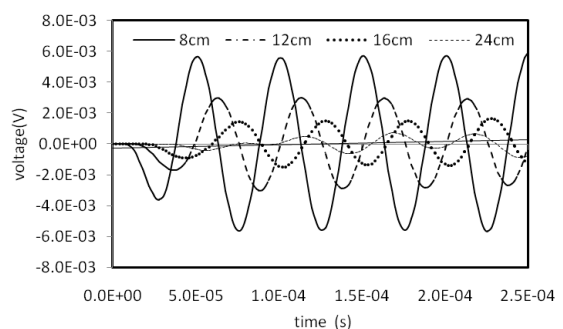


Fig. 9 Output voltage corresponding to different distances between the actuator and the sensor

$$V_{out} = K_1 A_x = K_2 A_0 e^{-\frac{1}{2}\alpha x} = 0.1 \times V_{input} \times 0.018 e^{-0.01x} \quad (26)$$

where A_x and A_0 stand for the signal amplitudes of sensor and actuator, α is the attenuation coefficient, x refers to the distance between transducers, K_1 and K_2 are proportional coefficients. V_{input} and V_{out} indicate the input and output voltages.

It is clear that the output of the embedded PZT sensor has a clear attenuation trend when the distance from the PZT sensor to the PZT actuator is less than the radius of the circular CFST member. As shown in Sections 3, when the distance is ranging from 24 cm to 40 cm, the superimposition of longitudinal wave, reflection wave and shear wave leads to a focal point. Therefore, appropriate arrangement for PZT transducers is necessary for the interface debonding detection of circular CFST members. It is suggested that for the interface debonding detection of a circular CFST member it is better to install the PZT sensor with a distance shorter than the radius of the CFST member.

The above findings are helpful for the determination of excitation signal frequency and the arrangement of the PZT sensors by considering the attenuation of signal with the excitation frequency and distance.

In the following section, the sensitivity of the PZT sensor measurement to the length and depth of the interface debonding defect under both sinusoidal signals and sweep frequency voltage signals is discussed respectively. The sweep frequency voltage signals employed is described in the following equations

$$V(t) = V_0 \sin[2\pi f(t)t] \quad (27)$$

$$f(t) = f_0 + \frac{f_1 - f_0}{T} t \quad (28)$$

where $V(t)$, V_0 refer to excitation voltage signal and its amplitude. $f(t)$, f_0 , f_1 stand for the frequency of signal at the time instant of t , initial frequency and final frequency, T is the time duration of the sweep frequency signal.

5.4.1 Under sinusoidal signal excitations

Here, the amplitude of input sinusoidal voltage is set to 10 V and the corresponding frequency is 20 kHz. The time duration of the excitation is set to 7.5 ms.

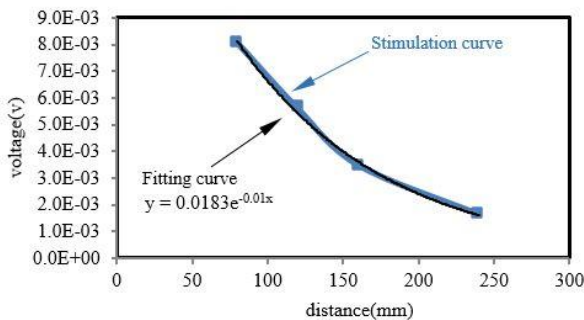


Fig. 10 The attenuation trend and the fitting curve

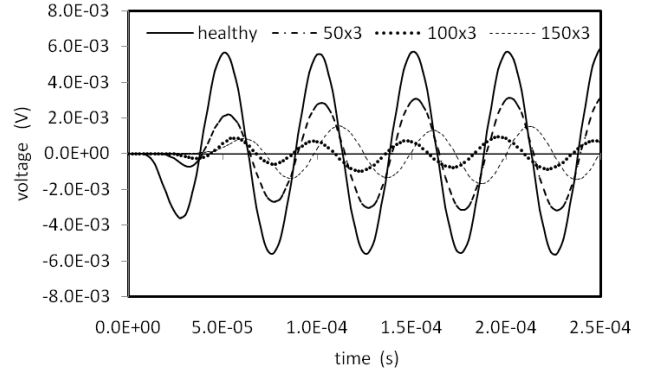


Fig. 11 Output voltage with different debonding lengths under sinusoidal excitation signal

The voltage outputs of the embedded PZT sensor are shown in Fig. 11. From Fig. 11, the difference in both the waveform amplitude and the corresponding arriving time of the head wave is clear due to different interface debonding lengths. The amplitude of the output voltage decays sharply due to the increase in the debonding length. Meanwhile, the arriving time of head wave in the circular CFST member delays when the the debonding length increases.

5.4.2 Under sweep frequency signal excitations

The sweep frequency signal with a frequency range from 5 kHz to 20 kHz and an amplitude of 10 V is employed to excite the coupling system. The time duration of the excitation is also set to 7.5 ms. The time domain waveforms of output voltage of the embedded PZT sensor in the circular CFST specimens with different debonding lengths are presented in Fig. 12.

As shown in Fig. 12, the output voltage waveform of the embedded PZT sensor in the circular CFST members with different defect lengths changes obviously. With the increase in defect length, the propagation path is prolonged. As a result, the traveling time of the head wave from the surface mounted PZT actuator to the embedded PZT sensor increases and the amplitude of the output has an obvious attenuation.

5.5 Sensitivity on interface debonding depths

Generally, interface debonding of CFST may initiate in the pouring process of concrete core or during the service period due to shrinkage of mass concrete. The initiation of debonding affects the mechanical behavior of CFST members. Debonding defect detection at early stage is crucial. In order to validate the sensitivity of PZT sensor measurement to the defect depth, circular CFST specimens with three kinds of debonding depths are considered while the defect length is 100 mm. The identical excitation voltage signals as them in Section 5.4 are employed.

5.5.1 Under sinusoidal signal excitation

The time-domain waveforms of the PZT actuator output voltage corresponding to different defect depths are shown in Fig. 13. As shown in Fig. 13(a), the amplitude of voltage signal of PZT sensor decreases obviously when the

interface dedonding defect occurs. But the wave forms corresponding to the interface debonding defect depth of 1 mm, 3 mm and 5 mm are very close. Fig. 13(b) gives a detail comparison of the output of the embedded PZT sensor of circular CFST members with different interface debonding depths. Compared with the output of the embedded PZT sensor in the healthy CFST member, the difference between them of the CFST members with different interface debonding depths is relatively small. This finding means that the response of the embedded PZT sensor under sinusoidal signal excitation is very sensitive to the initiation of debonding defect, but is not sensitive to the increase in the debonding depth. In other words, the PZT based interface debonding defect detection approach is very sensitive to the initiation of interface debonding for CFST members, which is important in practice and is very useful for the early age interface debonding monitoring of CFST members.

5.5.2 Under sweep frequency signal excitation

Under sweep frequency excitation signals, the output voltage signals corresponding to different defect depths are shown in Fig. 14. Similar conclusions as above can be drawn. As shown in Fig. 14(a), once interface debonding defect occurs, obvious variation of the output signal can be seen.

Fig. 14(b) shows the comparison of the embedded PZT sensor measurement of circular CFST members with different interface debonding depths. It can be found that the difference of the sensor measurement of circular CFST members with different interface debonding depths is not obvious even the amplitudes of the time-domain voltage decrease steadily along with the increase in debonding depth. From Fig. 14(b), the traveling time of head wave is prolonged correspondingly as well due to the increase in debonding depth. It is suggested that the sweep frequency signal is preferred in practical application since the PZT sensor under sweep frequency signal excitation provides response under excitation with a frequency range rather a signal frequency. In practice, the selection of the frequency range and time duration of the sweep frequency signals should be selected reasonably according to the dimensions of the circular CFST member and the possible interface debonding defect.

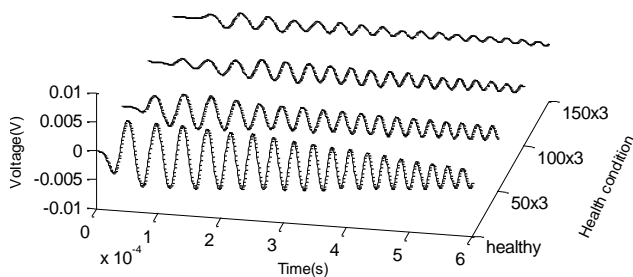
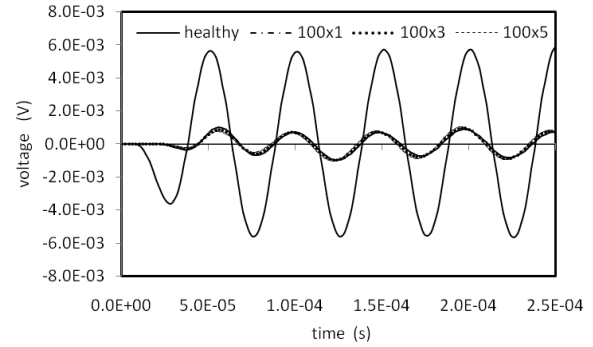
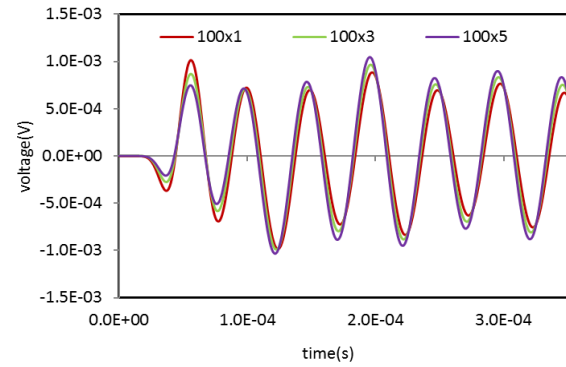


Fig. 12 Output voltage with different debonding lengths under sweep frequency excitation signal



(a) Comparison of healthy member with them with debonding defects of 100×1,100×3,100×5



(b) Comparison of members with interface debonding defects of 100×1,100×3,100×5

Fig. 13 Output voltage when debonding depth changes under sinusoidal excitation signal

6. Wavelet packet analysis on embedded PZT measurement and damage index

In order to quantitatively investigate the influence of debonding defect on the stress wave attenuation, wavelet packet analysis on the output voltage signals is carried out. An evaluation index based on the wavelet packet analysis results is defined to identify the interface debonding of circular CFST members.

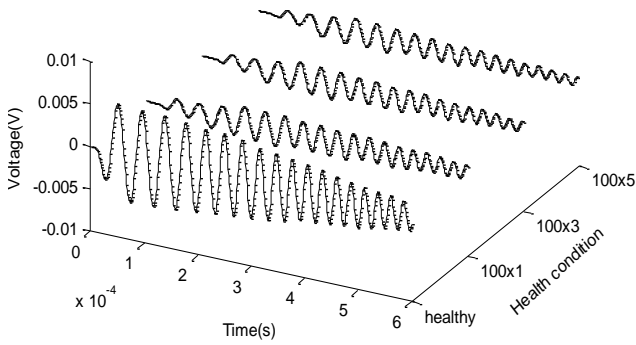
An initial voltage signal V of an embedded PZT sensor in the concrete core of a CFST member is decomposed by a N -level wavelet packet and then is further expressed as the summation of 2^N signal sets v_k . Therefore, the expressions of V and v_k can be described as follows (Chui 1992, Yen and Lin 1999)

$$V = v_1 + v_2 + \dots + v_k + \dots + v_{2^{N-1}} + v_{2^N}, \quad (29)$$

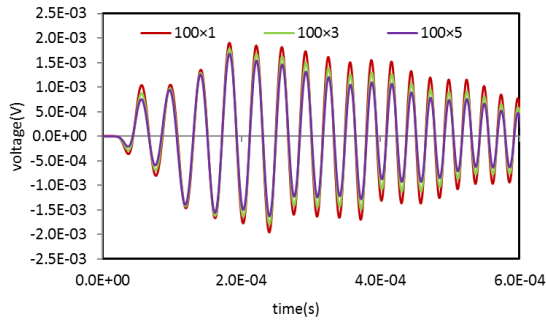
$$k = 1, 2, 3, \dots, 2^N$$

$$v_k = [v_{k,1}, v_{k,2}, \dots, v_{k,m}, \dots, v_{k,i-1}, v_{k,i}] \quad (30)$$

where $m = 1, 2, 3, \dots, i$, and i stand for the number of sampling data within the frequency band k .



(a) Comparison of healthy member with them with debonding defects of $100 \times 1, 100 \times 3, 100 \times 5$



(b) Comparison of members with interface debonding effects of $100 \times 1, 100 \times 3, 100 \times 5$

Fig. 14 Output voltage when debonding depth changes under sweep frequency excitation signal

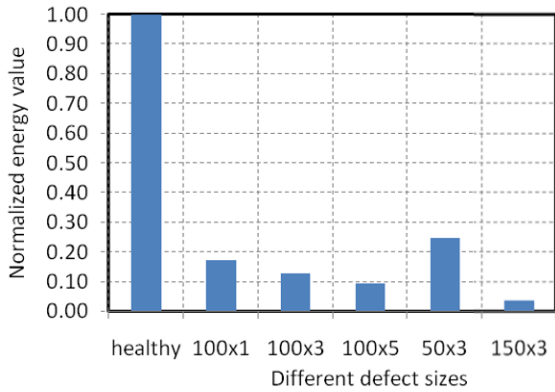


Fig. 15 NWPEI value corresponding to different interface debonding scenarios

After decomposition, an energy index of the original voltage signal can be further defined as follows

$$E = \sum_{k=1}^{2^N} e_k = \sum_{k=1}^{2^N} \left| \sum_{m=1}^i |v_{k,m}|^2 \right| \quad (31)$$

Then, a normalized wavelet packet energy index (NWPEI) is defined and employed as damage evaluation index for the interface debonding detection. The definition of the NWPEI is expressed as Eq. (32).

$$NWPEI = \frac{E_n}{E_{\max}}, (n = 1, \dots, j) \quad (32)$$

where E_{\max} and E_n correspond to the wavelet packet energy of voltage signal derived from the embedded PZT sensor in circular CTST members without and with debonding defect respectively. The number n corresponds to different debonding conditions as listed in Table 1.

In this study, the wavelet function 'db9' is adopted to carry out a three-level wavelet packet decomposition for the initial voltage signals according to Eqs. (29)-(32) and then the NWPEI is determined as shown in Fig. 15. Fig. 15 intuitively shows that the NWPEI gradually decreases with the increase of interface debonding dimension and is very sensitive to the initiation of the interface debonding.

7. Conclusions

In this paper, multi-physical coupling models composed of a surface mounted PZT actuator, an embedded PZT sensor and a circular CFST column section are constructed to numerically investigate the mechanism of stress wave measurement based interface debonding defect detection for circular CFST members. The initiation and propagation of the stress wave induced by the vibration of PZT actuator and the propagation pattern of stress wave in the cross section of the circular CFST members without and with debonding defect are discussed in details. The sensitivity of the embedded PZT sensor response to the debonding defect length and depth under both the sinusoidal and sweep frequency voltage signal excitations are discussed respectively. Based on the wavelet packet analysis on the response of the embedded PZT sensor, a normalized wavelet packet energy index (NWPEI) is defined for the interface debonding defect detection. The following conclusions can be made:

(1) Based on the multi-physical fields CFST-PZT coupling FE model, the linearity and stability of the voltage response of the embedded PZT sensor are verified. The amplitude relationship between input and output voltage, the attenuation trend with the increase of frequency and measurement distance are investigated respectively. The numerical simulation results are helpful for the selection of excitation signal parameters and PZT transducers arrangement in concrete core in practice.

(2) The initiation and propagation of the stress wave caused by the PZT actuator mounted at the surface of the circular steel tube of CFST members without and with debonding defect are compared, and the influence of the existence of the interface debonding on the wave initiation and propagation is analyzed.

(3) Sensitivity of the embedded PZT sensor voltage response to the debonding length and depth is investigated. Results indicate that embedded PZT sensor measurement under both sinusoidal voltage signal and sweep frequency voltage signal excitations is very sensitive to the initiation of debonding defect, which is meaningful in practice.

(4) In order to quantitatively evaluate the influence of debonding defect on the voltage response of the embedded PZT sensor, wavelet packet analysis on the time domain output voltage signals of the embedded PZT sensor corresponding to different debonding dimensions is carried

out and a normalized wavelet packet energy index (NWPEI) is defined and employed to detect the interfacial debonding defects of circular CFST structures. Results shows the NWPEI gradually decreases with the increase of damage dimension and much more sensitive to the initiation of interface debonding defects.

The findings from this study provide guidance in the excitation parameters selection and sensor arrangement for practice application and are helpful to understand the interfacial debonding defects detection mechanism of circular CFST members based on active PZT technology.

Acknowledgments

The authors gratefully acknowledge the support provided by the National Natural Science Foundation of China (NSFC) under grant No. 51261120374 and 51278185. The support provided by the Postgraduate Research and Innovation Project of Hunan Province under grant No. CX2016B104 to the second author is also appreciated.

References

- Bhalla, S. and Soh, C.K. (2004), "High frequency piezoelectric signatures for diagnosis of seismic/blast induced structural damages", *NDT & E Int.*, **37**(1), 23-33.
- China Engineering Construction standardization association (2000), *Technical Specification for Inspection of Concrete Defects by Ultrasonic Method*, China City Press, Beijing, China.
- Chui, C.K. (1992), *An Introduction to Wavelets*, Academic press, San Diego, CA, USA.
- COMSOL Inc.(2015), <http://cn.comsol.com/model/two-port-piezoelectric-saw-device-19155>.
- Feng, M.Q., De Flaviis, F. and Kim, Y.J. (2002), "Use of microwaves for damage detection of fiber reinforced polymer-wrapped concrete structures", *J. Eng. Mech. - ASCE*, **128**(2), 172-183.
- Gu, H.C., Moslehy, Y., Sanders, D., Song, G.B. and Mo, Y.L. (2010), "Multi-functional smart aggregate-based structural health monitoring of circular reinforced concrete columns subjected to seismic excitations", *Smart Mater. Struct.*, **19**(6), 322-328.
- Han, L. H., Li, W. and Bjorhovde, R. (2014). "Developments and advanced applications of concrete-filled steel tubular (CFST) structures: Members", *J. Constr. Steel Res.*, **100**, 211-228.
- Jung, Y.C., Kundu, T. and Ehsani, M.R. (2002), "A new nondestructive inspection technique for reinforced concrete beams", *ACI Mater. J.*, **99**(3), 292-299.
- Laskar, A., Gu, H.C., Mo, Y.L. and Song, G.B. (2009), "Progressive collapse of a two-story reinforced concrete frame with embedded smart aggregates", *Smart Mater. Struct.*, **18**(7), 5844-5877.
- Liu, P., Ho, G., Lee, A. and Yin, C. (2012), "Tianjin Goldin Finance 117 Tower: The Solution to a Slender Geometry", *Proceedings of the Council on Tall Buildings and Urban Habitat (CTBUH) 9th World Congress*, 801-808, Shanghai, September.
- Lu, Y, Ye, L., Su, Z.Q. and Yang, C.H. (2008), "Quantitative assessment of through-thickness crack size based on Lamb wave scattering in aluminium plates", *NDT & E Int.*, **41** (1), 59-68.
- Markovic, N., Nestorovic, T. and Stojic, D. (2015), "Numerical modeling of damage detection in concrete beams using piezoelectric patches", *Mech. Res. Commun.*, **64**, 15-22.
- Meng, Y.Y., Yan, S., Sun, W., Zhao, N.Z. and Qiu, G. (2010), "Experimental research on crack damage detection of concrete beam based on PZT wave method", *Proceedings of the SPIE - The International Society for Optical Engineering*, San Diego, CA, United states, March.
- Michaels, J.E. and Michaels, T.E. (2007), "Guided wave signal processing and image fusion for in situ damage localization in plates", *Wave Motion*, **44**(6), 482-492.
- Mo, X.P. (2007), "Simulation and analysis of acoustics transducers using the ANSYS software", *Technical Acoustics* **26**(6), 1279-1289.
- Morikawa, S.R.K., Gama, A.L. and Braga, A.M.B. and Correia, R.R. (2005), "Monitoring surface breaking defects with piezoelectric active systems", *Exper. Mech.*, **45**(1), 89-95.
- Moslehy, Y., Gu, H.C., Belarbi, A., Mo, Y.L. and Song, G.B. (2010), "Structural health monitoring of reinforced concrete columns subjected to reversed cyclic loading using innovative smart aggregates", *Proceedings of the 12th International Conference on Engineering, Science, Construction, and Operations in Challenging Environments-Earth and Space*, Honolulu, HI, United States, March.
- Olmi, C., Gu, H.C. and Song, G.B. (2007), "An overweight vehicle-bridge collision monitoring system using piezoelectric transducers", *Smart Mater. Struct.*, **16**(2), 462-468.
- Park, S., Ahmad, S., Yun, C.B. and Roh, Y. (2006), "Multiple crack detection of concrete structures using impedance-based structural health monitoring techniques", *Exper. Mech.*, **46** (5), 609-618.
- Song, G.B., Gu, H.C. and Mo, Y.L. (2008), "Smart aggregates: multi-functional sensors for concrete structures- a tutorial and a review", *Smart Mater. Struct.*, **17**(3), 847-854.
- Song, G.B., Gu, H.C., Mo, Y.L., Hsu, T. T. C. and Dhonde, H. (2007), "Concrete structural health monitoring using embedded piezoceramic transducers", *Smart Mater. Struct.*, **16**(4), 959-968.
- Wang, D.S., Song, H.Y. and Zhu, H.P. (2013), "Numerical and experimental studies on damage detection of a concrete beam based on PZT admittances and correlation coefficient", *Constr. Build. Mater.*, **49**, 564-574
- Wang, D.S., Song, H.Y. and Zhu, H.P. (2014), "Embedded 3-D electromechanical impedance model for strength monitoring of concrete using PZT transducer", *Smart Mater. Struct.*, **23**, 115019
- Wang, Z.P. (2013), "Research on the theory and technology of ultrasonic linear phased array actuator applied in structural damage detection", Ph.D. Dissertation, Jiangsu University, Zhenjiang.
- Wu, F. and Chang, F.K. (2006a), "Debond detection using embedded piezoelectric elements for reinforced concrete structures-Part II: Analysis and algorithm", *Struct. Health Monit.*, **5**(1), 17-28.
- Wu, F. and Chang, F.K. (2006b), "Debond detection using embedded piezoelectric elements in reinforced concrete structures-Part I: Experiment", *Struct. Health Monit.*, **5**(1), 5-15.
- Xu, B., Li, B. and Song, G.B. (2013), "Active debonding detection for large rectangular CFSTs based on wavelet packet energy spectrum with piezoceramics", *J. Struct. Eng. - ASCE*, **139**(9), 1435-1443.
- Xu, B., Li, B. Song, G.B. Teng J. and LingHu, Y. (2012), "Detection of the debonding defect of concrete-filled steel tubes with piezoceramics", *Tumu Gongcheng Xuebao/China Civil Eng. J.*, **45**(7), 86-96.
- Xu, B., Zhang, T., Song, G.B. and Gu, H.C. (2013), "Active interface debonding detection of a concrete-filled steel tube with piezoelectric technologies using wavelet packet analysis", *Mech.*

- Syst. Signal Pr.*, **36**(1), 7-17.
- Xue, J.Q., Briseghella, B. and Chen, B.C. (2012), "Effects of debonding on circular CFST stub columns", *J. Constr. Steel Res.*, **69**(1), 64-76.
- Yan, S., Sun, W., Meng, Y.Y., Ni, P. and Liu, Z. (2009), "Crack monitoring for reinforced concrete columns based on piezoceramic transducers", *Proceedings of SPIE-The International Society for Optical Engineering*, San Diego, CA, United states, March.
- Yang, C.H., Ye, L. and Su, Z.Q., Bannister, M. (2006), "Some aspects of numerical simulation for Lamb wave propagation in composite laminates", *Compos. Struct.*, **75**(1), 267-275.
- Yen, G.G. and Lin, K.C. (1999), "Wavelet packet feature extraction for vibration monitoring", *IEEE T. Ind. Electron.*, **47**(3), 650-667.
- Zhao, X.Y. and Li, H.N. (2006), "Health monitoring of reinforced concrete frame-shear wall using piezoceramic transducer", *Zhendong yu Chongji/J. Vibration and Shock*, **25**(4), 82-84+93.
- Zhao, X.Y. and Li, H.N. (2009), "Piezoelectric-based monitoring of concrete crack damage", *Piezoelectric Acousto-optic*, **31**(3), 437-439+443.

BS